

1 **Improvement of Near-field Tsunami Forecasting Method Using Ocean Bottom Pressure**  
2 **Sensor Network (S-net)**

3

4 Yuichiro Tanioka<sup>1</sup>

5 <sup>1</sup> Institute of Seismology and Volcanology, Hokkaido University, N10W8 Kita-ku Sapporo,  
6 Hokkaido 060-0810, Japan. e-mail: tanioka@sci.hokudai.ac.jp

7

8

9

10 **Abstract**

11 Since the installation of a dense cabled observation network around the Japan Trench (S-net) by  
12 the Japanese government that includes 150 sensors, several tsunami forecasting methods that use  
13 the data collected from the ocean floor sensors were developed. One of such methods is the tsunami  
14 forecasting method which assimilates the data without any information of earthquakes. The  
15 tsunami forecasting method based on the assimilation of the ocean-bottom pressure data near the  
16 source area was developed by Tanioka in 2018. However, the method is too simple to be used for  
17 an actual station distribution of S-net. To overcome its limitation, we developed an interpolation  
18 method to generate the appropriate data at the equally spaced positions for the assimilation from  
19 the data observed at sensors in S-net. The method was numerically tested for two large underthrust  
20 fault models, a giant earthquake (Mw8.8) and the Nemuro-oki earthquake (Mw8.0) models. Those  
21 fault models off Hokkaido in Japan are expected to be ruptured in the future. The weighted  
22 interpolation method, in which weights of data are inversely proportional to the square of the  
23 distance, showed good results for the tsunami forecast method with the data assimilation.

24 Furthermore, results indicated that the method is applicable to the actual observed data at the S-  
25 net stations. The only limitation of the weighted interpolation method is that the computed tsunami  
26 wavelengths tend to be longer than the actual tsunamis wavelength.

27

28 **Keywords:**

29 tsunami forecasting method, data assimilation, tsunami numerical simulation, Kurile subduction  
30 zone.

31

32 **1. Introduction**

33 The 2011 Tohoku-oki earthquake (Mw9.0) generated a large tsunami along the Pacific coast of  
34 northern Japan (Mori et al., 2012). Although the Japan Meteorological Agency (JMA) issued a  
35 major tsunami warning along the Pacific coast of Japan immediately after the earthquake (Ozaki,  
36 2011), the tsunami caused a catastrophic disaster with approximately 19,000 casualties. After this  
37 event, the development of a more accurate and rapid tsunami warning system became a high-  
38 priority focus area in Japan.

39 For this purpose, the Japanese government installed a dense cabled observation network, called  
40 the seafloor observation network for earthquakes and tsunami around the Japan Trench (S-net), in  
41 2017. The network is operated by the National Research Institute for Earth Science and Disaster  
42 Resilience (NEID). In this network, 150 observation stations consisting of ocean-bottom pressure  
43 sensors and seismometers are connected by cables at the 30-km intervals (Uehira et al.,2012;  
44 Kanazawa, 2013). The cables are distributed on the seafloor offshore off northern Japan (Figure  
45 1).

46 Recently, various early forecasting methods for tsunami using the dense seafloor observation  
47 networks have been proposed. Tsushima et al. (2012) developed a method called tsunami  
48 Forecasting based on Inversion for initial sea Surface Height (tFISH) which estimates the initial  
49 sea surface deformation from tsunami waveforms observed at ocean bottom pressure gauges.  
50 Yamamoto et al. (2016) developed a tsunami forecasting method that rapidly estimates tsunami  
51 inundation based on a multi-index method and compares the observed tsunami heights with the  
52 pre-computed tsunami heights at ocean bottom sensors. Moreover, new tsunami computation  
53 methods based on the assimilation of tsunami observations without the tsunami source information  
54 were developed by Maeda et al., (2015), Tanioka (2018), and Tanioka and Gusman (2018).  
55 Gusman et al. (2016) applied the method developed by Maeda et al. (2015) to the tsunami  
56 generated by the 2012 Haida Gwaii earthquake and computed the tsunami wave field successfully  
57 by assimilating data observed at ocean bottom pressure sensors in Cascadia. However, this method  
58 is difficult to apply to ocean bottom pressure data within the source area because the ocean surface  
59 displacement above the source area just after the earthquake cannot be observed by the ocean bottom  
60 pressure sensors. The near-field tsunami inundation forecasting method developed by Tanioka  
61 (2018) and Tanioka and Gusman (2018) uses the time derivative of the pressure waveforms  
62 observed at the ocean bottom pressure sensors near the source area. Therefore, tsunami  
63 computation by assimilating data can be performed without any tsunami source information as  
64 soon as the earthquake or tsunami generation is completed. Tanioka and Gusman (2018) tested  
65 ocean-bottom pressure sensors equally distributed at 15 min intervals or approximately 30 km  
66 apart. In reality, the S-net ocean-bottom sensors are not installed at uniform intervals (Figure 1),  
67 particularly in the north-south direction, and have a lesser number than those tested by Tanioka

68 and Gusman (2018). They finally concluded that it is necessary to improve their method by using  
 69 the exact locations of the S-net sensors for real time tsunami inundation forecasts.

70 In this paper, we improve the tsunami forecasting method proposed by Tanioka (2018) and  
 71 Tanioka and Gusman (2018) to be able to use the exact locations of the S-net sensors. This  
 72 improved method was tested for two expected large underthrust earthquakes off the Pacific coast  
 73 of Hokkaido, Japan: an expected magnitude 9 class earthquake, and the Nemuro-oki earthquake  
 74 with a magnitude of 8.

75

## 76 2. Previous Method to Determine the Tsunami Height Field

77 Tanioka (2018) presented a tsunami simulation method that assimilates dense ocean bottom  
 78 pressure data near the tsunami source regions. Tanioka and Gusman (2018) suggested a near-field  
 79 tsunami inundation forecasting method based on the method presented by Tanioka (2018). Here,  
 80 we briefly explain the method used to determine the tsunami height field. A governing equation  
 81 for the tsunami propagation, the wave equation of the linear shallow-water approximation, is as  
 82 follows:

$$83 \quad \frac{\partial^2 h_f(x,y,t)}{\partial t^2} = \frac{\partial^2 \eta(x,y,t)}{\partial t^2} = gd \left( \frac{\partial^2 \eta(x,y,t)}{\partial x^2} + \frac{\partial^2 \eta(x,y,t)}{\partial y^2} \right), \quad (1)$$

84 where  $d$  is the depth of the ocean,  $\eta(x,y,t)$  is the ocean surface displacement or tsunami height  
 85  $h_f(x,y,t)$  is the water depth fluctuation proportional to the ocean-bottom pressure change

86  $\Delta p(x,y,t)$  as:  $h_f(x,y,t) = \frac{1}{\rho g} \Delta p(x,y,t)$  where  $\rho$  is the density of sea water and  $g$  is the

87 gravitational acceleration. From Eq. (1) the finite difference equation is obtained as follows:

$$88 \quad \frac{h_{f_{i,j}}^{k+1} - 2h_{f_{i,j}}^k + h_{f_{i,j}}^{k-1}}{\Delta t^2} = gd_{i,j} \left( \frac{\eta_{i+1,j}^k - 2\eta_{i,j}^k + \eta_{i-1,j}^k}{\Delta x^2} + \frac{\eta_{i,j+1}^k - 2\eta_{i,j}^k + \eta_{i,j-1}^k}{\Delta y^2} \right), \quad (2)$$

89 where  $i$  and  $j$  are indices of points for the x- and y-directions in the computed domain,  $k$  is the  
90 index for time steps,  $\Delta x$  and  $\Delta y$  are the spacing intervals in the x and y directions, respectively,  
91 and  $\Delta t$  is the time interval. Afterwards, we assumed that there were hypothetical pressure sensors  
92 at each point (marked in red dots in Figure 2). The spacing interval for both the x and y directions  
93 is 10 arc-min or approximately 18 km. As such, the total number of hypothetical sensors was  
94 assumed to be 275. The left-hand side of Eq. (2) was obtained from the pressure data at each  
95 hypothetical pressure sensor. The unknown parameters were ocean surface displacement field or  
96 tsunami height field,  $\eta_{i,j}^k$ , above each hypothetical pressure gauge at a particular time,  $k$ . The  
97 tsunami heights outside the hypothetical pressure gauge network were assumed to be 0.  
98 Subsequently, we were able to compute the tsunami height field,  $\eta_{i,j}^k$ , above the hypothetical  
99 pressure sensor network by solving Eq. (2) for all hypothetical pressure sensors by using the  
100 inversion technique as described by Tanioka (2018).

101

### 102 3. Interpolation Method for Data Assimilation

103 A problem with the method mentioned above is that in practice, the S-net sensors are not  
104 distributed at the 10 arc-min intervals in the x and y direction, and the number of the S-net sensors  
105 is much less than 275 (Figure 2). To solve this problem, we need to develop an appropriate  
106 interpolation method to obtain pressure data at the hypothetical points situated at the 10 arc-min  
107 intervals (red dots in Figure 2) from the observed pressure data at the S-net sensors (black dots in  
108 Figure 2). A number of weighted interpolation methods were tested to find the most appropriate  
109 one. The left-hand side of Eq. (2),  $z_p^k = \frac{h_{f_p}^{k+1} - 2h_{f_p}^k + h_{f_p}^{k-1}}{\Delta t^2}$ , at each sensor position  $(x_p, y_p)$  in S-net  
110 was calculated from the observed pressure data. The left-hand side of Eq. (2),  $z_{i,j}^k =$

111  $\frac{h_{f_{i,j}}^{k+1} - 2h_{f_{i,j}}^k + h_{f_{i,j}}^{k-1}}{\Delta t^2}$ , at each hypothetical point  $(x_{i,j}, y_{i,j})$  at the 10 arc-min intervals (red dots in Figure

112 2) was obtained by the weighted interpolation equation as follows:

113

$$114 \quad z_{i,j}^k = \frac{\sum_{p=1}^n w_{p,i,j} z_p^k}{\sum_{p=1}^n w_{p,i,j}} \quad (3)$$

115

116 where  $w_{p,i,j}$  is the weight factor for each observed point ( $p$ ) to calculate  $z_{i,j}^k$  at each hypothetical  
117 point ( $i, j$ ). Then, the weight factor was defined as follows:

$$118 \quad w_{p,i,j} = \frac{1}{\left(\sqrt{(x_p - x_{i,j})^2 + (y_p - y_{i,j})^2}\right)^\alpha} \quad (4)$$

119 where  $\alpha$  is the control factor. If control factor  $\alpha$  equals one, the weights are inversely proportional  
120 to the distance between the observed points in S-net and hypothetical points for assimilation. In  
121 this study, we varied control factor  $\alpha$  from 1 to 3 (integers only) to find the best factor that provides  
122 an appropriate tsunami height distribution near a tsunami source area using the assimilation  
123 technique developed by Tanioka (2018).

124

#### 125 **4. Test Region and Fault Models**

126 Great underthrust earthquakes repeatedly occurred in the past at the plate interface in the  
127 subduction zone where the Pacific plate subducts beneath the Kurile Trench off Hokkaido (Figure  
128 1). Historically, the Pacific coast of Hokkaido has suffered from large disasters due to those  
129 earthquakes and their associated tsunamis (Tanioka et al., 2007). Additionally, the paleo-  
130 earthquake studies using tsunami deposits along the Pacific coast of Hokkaido revealed that much  
131 larger tsunamis repeatedly occurred in the past 6000 years compared with historical tsunamis

132 (Nanayama et al., 2003; Hirakawa et al, 2005). The most recent large paleo-tsunami that occurred  
133 in the early 17<sup>th</sup> century (Figure 1) was well studied by Satake et al., (2008) and Ioki and Tanioka  
134 (2016). The fault model of the earthquake was constructed by reproducing the observed tsunami  
135 deposit distribution along the Hokkaido coast with the computed one. Ioki and Tanioka (2016)  
136 concluded that the great underthrust earthquake with a moment magnitude of 8.8 ruptured a large  
137 area of the plate interface off Hokkaido. The Headquarters for Earthquake Research Promotion,  
138 Japan, published a long-term evaluation report on the occurrence of large subduction earthquakes  
139 along the Kurile Trench (Headquarters of Earthquake Research Promotion, 2018). They reported  
140 that the probability of a giant earthquake with a magnitude exceeding Mw 8.8 along the Kurile  
141 trench in 30 years is between 7% and 40%. Therefore, mitigation of tsunami disasters due to the  
142 giant earthquake (M8.8) has become an urgent challenge in Japan, particularly in Hokkaido.

143 In this study, we chose the hypothetical giant earthquake (Mw8.8) along the Kurile trench off  
144 Hokkaido to test our tsunami simulation by assimilating pressure data observed by the S-net  
145 sensors near the source region. The fault length and fault width for this hypothetical earthquake  
146 (Figure 2) were set to be 300 km and 100 km, respectively, as per the estimations of the 17<sup>th</sup>-  
147 century giant earthquake fault model (Satake et al., 2008; Ioki and Tanioka, 2016). A strike of  
148 228°, a dip of 15°, and a rake of 90° were set to be the same as those in the 17<sup>th</sup>-century giant  
149 earthquake fault model (Table 1). A slip amount was calculated to be 15 m by assuming a moment  
150 magnitude of 8.8 and a rigidity of  $4 \times 10^{10}$  N/m<sup>2</sup>.

151 The Headquarters for Earthquake Research Promotion also reported that the probability of a  
152 great Nemuro-oki earthquake (Mw7.8-8.5) along the Kurile trench in 30 years is approximately  
153 70%, being higher than that of the giant earthquake (Mw8.8). In this region, the 1973 Nemuro-oki  
154 earthquake (Mw 7.8) (Figure 1) and the 1894 Numuro-oki earthquake (Mw8.2) were previously

155 occurred. Tanioka et al. (2007) showed that the fault size of the 1894 event (200km x 100 km) was  
156 larger than that of the 1973 event (80 km x 80 km). In this study, we chose the Nemuro-oki  
157 earthquake (Mw 8.0) to test our method. The fault length and fault width of the earthquake (Figure  
158 2) were set to be 100 km and 80 km, respectively. A strike of 240°, a dip of 15°, and a rake of 90°  
159 were set the same as those in the fault model of the Nemuro-oki earthquakes (Table 1). A slip  
160 amount was calculated to be 4 m by assuming a moment magnitude of 8.0 and a rigidity of 4 x  
161 10<sup>10</sup> N/m<sup>2</sup>.

162

## 163 **5. Method for Numerical Computation Tests**

164 Two reference tsunamis, used as the original tsunamis for synthetic tests, were computed in the  
165 area off Hokkaido and Tohoku (Figure 2). The coseismic vertical deformation was calculated using  
166 the Okada's (1985) equations from the fault models of the two reference earthquakes (Table 1)  
167 and used as the initial conditions of tsunamis. The tsunamis were numerically computed by solving  
168 the linear long-wave equations by using the finite difference method with a staggered grid system  
169 (Satake, 2015). The grid size of the tsunami computation was set at 1 arc-min (approximately  
170 1.8 km). The time step of the computation was set to be 2 s to satisfy the stability condition. The  
171 duration of the earthquake was chosen to be 90 seconds.

172 To test the assimilation method, the tsunami waveforms at the S-net observation points (black  
173 dots in Figure 2) were computed numerically from the reference fault models and transferred to  
174 the water-depth fluctuation,  $h_f(x,y,t)$  in Eq. (1), as described in Tanioka (2018). Afterwards, the

175 left-hand side of Eq. (2),  $z_p^k = \frac{h_f^{k+1} - 2h_f^k + h_f^{k-1}}{\Delta t^2}$ , at each sensor position ( $x_p, y_p$ ) in S-net at a time

176  $k$  was calculated from the water-depth fluctuation data. Time intervals,  $\Delta t$ , for the giant earthquake  
177 (Mw8.8) and the Nemuro earthquake (Mw8.0) cases were set at 6 s and 30 s, respectively. Time

178 interval,  $\Delta t$ , needs to be larger for a smaller earthquake because term,  $h_p^{k+1} - 2h_p^k + h_p^{k-1}$ , needs  
179 to be large enough to be observed at the S-net sensors. Then, those at equally distributed  
180 hypothetical points  $(x_{i,j}, y_{i,j})$  at the 10 arc-min intervals (red dots in Figure 2),  $z_{i,j}^k =$   
181  $\frac{h_{i,j}^{k+1} - 2h_{i,j}^k + h_{i,j}^{k-1}}{\Delta t^2}$ , were obtained by the above interpolation methods. Subsequently, the tsunami  
182 height fields at equally distributed hypothetical points at a time  $k$  were computed using the  
183 assimilation method as described by Tanioka (2018). For tsunami simulation, the tsunami height  
184 field obtained at a time  $k$  from the observed depth fluctuation data at the S-net sensors replaced  
185 the tsunami height field at a time  $k$  during the tsunami numerical simulation. The replacements of  
186 the tsunami height field as data assimilations were completed at 90 s after the initiation of the  
187 earthquake as the duration of the earthquake was set at 90 s. Finally, the tsunami numerical  
188 simulation was continued until 90 min after the earthquake by solving the linear long-wave  
189 equations without data assimilation.

190

## 191 6. Results

192 In the first test case, a tsunami caused by the giant earthquake (Mw8.8) along the Kurile Trench  
193 off Hokkaido was numerically computed as a reference tsunami. The computed tsunami height  
194 fields at 90 and 1200 s after the initiation of the earthquake are shown in Figure 3. The tsunami  
195 height fields were computed by the assimilation of simulated observation data at sensors in S-net  
196 (Figure 2) using the interpolation method utilized in Eqs. (3) and (4) with three control factors ( $\alpha$   
197 = 1, 2, and 3) (Figure 3). Seven computed tsunami waveforms at Hanasaki, Kushiro, Hiroo, and  
198 Urakawa in Hokkaido, and Hachinohe, Miyako, and Kesenuma in Tohoku obtained from the  
199 reference tsunami and from the assimilations using the interpolation with three control factors ( $\alpha$   
200 =1, 2, and 3) are compared in Figure 4. The maximum tsunami heights at these seven locations are

201 also presented in Table 2. The tsunami waveforms (Figure 4) and maximum tsunami heights (Table  
202 2) from the reference tsunami computation were comparable to those from the assimilation of  
203 simulated observation data using the interpolation, where control factor  $\alpha$  equaled two. The  
204 maximum tsunami heights computed from the assimilation of the data using the interpolation,  
205 where control factor  $\alpha$  equaled one, were underestimated compared to the maximum tsunami  
206 heights computed directly from the reference fault model. Some of the tsunami waveforms from  
207 the assimilation of those data were different from those of the reference model, especially the  
208 waveforms at Hanasaki in Hokkaido. On the contrary, the maximum tsunami heights computed  
209 from the assimilation of the data using interpolation, where control factor  $\alpha$  equaled 3, were  
210 overestimated in comparison with those computed directly from the reference fault model.  
211 Therefore, we conclude that the weighted interpolation method, where control factor  $\alpha$  equaled  
212 two in Eq. (4), is appropriate for our assimilation method using the ocean-bottom pressure data  
213 observed at the S-net sensors.

214 As for the second test case, the tsunami caused by the fault model of the Nemuro-oki earthquake  
215 (Mw 8.0) was numerically computed as a reference tsunami. The computed tsunami height fields  
216 at 90 and 1200 s after the initiation of the earthquake are shown in Figure 5a. The tsunami height  
217 fields were computed by the assimilation of simulated observation data at the S-net sensors (Figure  
218 2) using the interpolation method as described by Eq. (3), where control factor  $\alpha$  equaled two  
219 (Figure 5b). Seven computed tsunami waveforms from the reference tsunami and from the data  
220 assimilations using the interpolation are compared in Figures 6a-b. The maximum tsunami heights  
221 at these seven locations are also presented in Table 3. As the assimilation area was much larger  
222 than the source area in this case, small tsunami height fields in the southwest of the assimilation  
223 area, where no tsunami was computed as a reference tsunami, were realized for the data

224 assimilation (Figure 5b). Therefore, the computed tsunami waveforms from the data assimilation  
225 using the interpolation (Figure 6b) have longer period characteristics and higher maximum tsunami  
226 heights than those waveforms of the reference tsunami. These results indicate that the data  
227 assimilation area needs to be limited to an area with reasonable water depth fluctuations observed  
228 at the S-net sensors.

229 Furthermore, we used a small assimilation area shown in Figure 7. For sensors in this small  
230 assimilation area, the calculated assimilation data  $z_p^k = \frac{h_p^{k+1} - 2h_p^k + h_p^{k-1}}{\Delta t^2}$  were more than 1/20 of  
231 the maximum assimilation data of all the sensors. The computed tsunami height fields at 90 and  
232 1200 s after the initiation of the earthquake are shown in Figure 5c. Figure 6 shows that seven  
233 computed tsunami waveforms from the reference tsunami are better fitted by the computed tsunami  
234 waveforms from the data assimilation in the small area using interpolation than in the large area.  
235 Table 3 also shows that the maximum tsunami heights of the reference tsunami better agree with  
236 those computed from the data assimilation in the small area than in the large area.

237

## 238 7. Discussion

239 The case study for the Nemuro-oki earthquake (Mw 8.0) showed that the reference tsunami better  
240 agreed with the computed tsunami using the small assimilation area limited to the tsunami source  
241 area. It is better to check this effect for the giant earthquake (Mw 8.8) case. We recomputed the  
242 tsunami height field using the largest assimilation area shown in Figure 8a by the assimilation of  
243 simulated observation data at the S-net sensors using the interpolation method as described by Eq.  
244 (3), where control factor  $\alpha$  equaled two. The computed result was compared with the previous  
245 result using the assimilation area shown in Figure 2 for the giant earthquake (Mw 8.8) case (Figure  
246 3 and 4). The computed tsunami height fields at 90 after the initiation of the earthquake (Figure

247 8b) is almost the same as the result shown in Figure 3 for the control factor,  $\alpha$  equaled two. Figure  
248 8c shows that seven computed tsunami waveforms using the largest assimilation area are almost  
249 same as those computed waveforms using the assimilation area shown in Figure 2. Those results  
250 indicated that the effect of limiting a size of the assimilation area is negligible to be consider for  
251 the giant earthquake (Mw 8.8) case and only significant for the Nemuro-oki earthquake (Mw 8.0)  
252 case which has a smaller tsunami source area than the giant earthquake case.

253 To use our improved assimilation method in practice, non-tsunami components such as sea-  
254 bottom acceleration changes due to a fault motion of an earthquake should be removed from the  
255 original ocean bottom pressure data. Saito and Tsushima (2016) showed that the first ~90 s of  
256 ocean bottom pressure data is highly affected by acoustic waves and seismic waves generated by  
257 the earthquake. Mizutani et al. (2020) recently developed an early tsunami detection method for  
258 near-fault ocean bottom pressure data by comparing the seismic data and pressure data at the same  
259 site to eliminate non-tsunami components. This tsunami detection method should be applied to  
260 original pressure data before our improved assimilation method is applied to the data. Another  
261 difficulty for practical use of our method is that the end of the earthquake rupture is unknown.  
262 Although replacements of the tsunami height field as data assimilations were completed at 90 s in  
263 this study, those replacements should continue more than the duration of the earthquake in practice.  
264 We may need to decide the ending time of those replacements using the seismic records at the  
265 same sites as the pressure observations. Finally, after pressure sensors are suffered by the strong  
266 motion of a large earthquake, mechanical malfunction of the sensors may occur as suggested by  
267 Kubota et al. (2018). Those sensors need to be found as soon as the strong motion ends to eliminate  
268 the data at those sensors from the assimilation data in our method.

269

270 **8. Conclusion**

271 We developed a tsunami forecasting method using the assimilation of data obtained by  
272 interpolation of observed data at the S-net sensors near the tsunami source area. The interpolation  
273 method, as described in Eq. (3), where control factor  $\alpha$  equaled two, performed acceptable for the  
274 tsunami forecasting method for the giant earthquake case. However, for the Nemuro-oki  
275 earthquake (Mw 8.0) case, the wavelengths of tsunami waveforms computed using the assimilation  
276 of data were slightly longer and larger than those of the reference tsunami. This indicates the  
277 limitation of data assimilation using the suggested interpolation method because assimilation data  
278 at 176 points (red dots in Figure 7) were calculated from the interpolation of data at only 12 S-net  
279 sensors for the Nemuro-oki earthquake case. Then, the assimilation area should be limited to an  
280 area where the reliable water depth fluctuations are observed at the S-net sensors. Moreover,  
281 tsunami height fields from a smaller earthquake are more difficult to be computed using our data  
282 assimilation method.

283

284 **Acknowledgments**

285 We would like to thank Editage ([www.editage.com](http://www.editage.com)) for English language editing. This study was  
286 supported by JSPS KAKENHI Grant Number 18H03819.

287

288 **Abbreviations**

289 **S-net:** Seafloor observation network for earthquake and tsunami along the Japan Trench

290 **JMA:** Japan Meteorological Agency

291 **fFISH:** tsunami Forecasting based on Inversion for initial sea Surface Height

292 **Availability of data and materials:**

293 None

294 **Competing interests:**

295 None

296 **Funding**

297 This study was supported by JSPS KAKENHI Grant Number 18H03819.

298 This study was also supported by the Ministry of Education, Culture, Sports, Science and  
299 Technology (MEXT) of Japan, under its The Second Earthquake and Volcano Hazards  
300 Observation and Research Program (Earthquake and Volcano Hazard Reduction Research)

301 **Authors' contributions**

302 Y.T did all.

303

304 **References**

305 Gusman, R. G., A. F. Sheehan, K. Satake, M. Heidazadeh, I. E. Mulia, and T. Maeda, (2016),  
306 Tsunami data assimilation of Cascadia seafloor pressure gauge records from the 2012 Haida  
307 Gwaii earthquake, *Geophy. Res. Lett.*, doi:10.1002/2016GL068368.

308 Headquarters of Earthquake Research Promotion (2018), Evaluations of occurrence potential of  
309 large earthquakes along the Kurile trench, [https://www.jishin.go.jp/main/chousa/kaikou\\_pdf/  
310 chishima3.pdf](https://www.jishin.go.jp/main/chousa/kaikou_pdf/chishima3.pdf) (in Japanese)

311 Hirakawa, K., Y. Nakamura, Y. Nishimura (2005), Mega-Tsunamis since last 6500 years along  
312 the Pacific Coast of Hokkaido, Special Issue, *Chikyū Monthly*, 49, 173-180 (in Japanese)

313 Imamura, F. (1996). Review of tsunami simulation with a finite difference method, in *Long-Wave  
314 Runup Models*, edited by H. Yeh, P. Liu, and C. Synolakis, 403 pp., *World Scientific*,  
315 Singapore.

316 Ioki, K., and Y. Tanioka (2016), Re-estimated fault model of the 17th century great earthquake off  
317 Hokkaido using tsunami deposit data, *Earth Planet. Sci. Lett.*, 433, 133-138,  
318 <https://doi.org/10.1016/j.epsl.2015.10.009>

319 Kanazawa, T. (2013), Japan Trench earthquake and tsunami monitoring network of cable-linked  
320 150 ocean bottom observatories and its impact to earth disaster science, *Proceedings of the*  
321 *International Conference Underwater Technology*.

322 Kubota, T., W. Suzuki, T. Nakamura, N. Y. Chikasada, S. Aoi, N. Takahashi, and R. Hino (2018),  
323 Tsunami source inversion using time-derivative waveform of offshore pressure records to  
324 reduce effects of non-tsunami components. *Geophysical Journal International*, 215(2), 1200-  
325 1214.

326 Maeda, T., K. Obara, M. Shinohara, T. Kanazawa, and K. Uehira (2015), Successive estimation  
327 of a tsunami wavefield without earthquake source data: A data assimilation approach toward  
328 real-time tsunami forecasting, *Geophys Res Lett*, 42(19), 7923–7932.

329 Mizutani, A., K. Yomogida, and Y. Tanioka (2020), Early tsunami detection with near-fault ocean-  
330 bottom pressure gauge records based on the comparison with seismic data, *Journal of*  
331 *Geophysical Research: Oceans*, <https://doi.org/10.1029/2020JC016275>.

332 Mori N, Takahashi T, The 2011 Tohoku earthquake tsunami joint survey group (2012) Nationwide  
333 post event survey and analysis of the 2011 Tohoku earthquake tsunami. *Coastal Eng J*  
334 54(1):1250001. <https://doi.org/10.1142/S0578563412500015>

335 Nanayama, F., K. Satake, R. Furukawa, K. Shimokawa, B.F. Atwater, K. Shigeno, and S. Yamaki  
336 (2003) Unusually large earthquakes inferred from tsunami deposits along the Kurile trench,  
337 *Nature*, 424, 660-663

338 Okada, Y. (1986). Surface deformation due to shear and tensile faults in a half-space. *Bulletin of*  
339 *the Seismological Society of America*, 75, 1135-1154.

340 Ozaki, T. (2011), Outline of the 2011 off the Pacific coast of Tohoku earthquake (Mw 9.0) -  
341 Tsunami warnings/advisories and observations, *Earth Planets Space*, 63(7), 827– 830

342 Saito, T., and H. Tsushima (2016), Synthesizing ocean bottom pressure records including seismic  
343 wave and tsunami contributions: Toward realistic tests of monitoring systems. *Journal of*  
344 *Geophysical Research: Solid Earth*, 121(11), 8175-8195.

345 Satake, K. (2015). *Tsunamis, in treatise on geophysics, vol 4* (2nd ed., pp. 477–504. Amsterdam:  
346 Elsevier.

347 Satake, K., F. Nanayama, and S. Yamaki (2008), Fault models of unusual tsunami in the 17th  
348 century along the Kurile trench, *Earth Planets Space*, 60, 925-935.

349 Tanioka, Y., K. Satake, and K. Hirata (2007), Recurrence of Recent Large Earthquakes Along the  
350 Southernmost Kurile-Kamchatka Subduction Zone, *Geophysical monograph*, 172, 145-152.

351 Tanioka, Y. (2018), Tsunami Simulation Method Assimilating Ocean Bottom Pressure Data Near  
352 a Tsunami Source Region, *Pure Appl Geophys*, 175(2), 721–729.

353 Tanioka, Y. and A.R. Gusman, (2018) Near-field tsunami inundation forecast method assimilating  
354 ocean bottom pressure data: A synthetic test for the 2011 Tohoku-oki tsunami, *Phys. Earth*  
355 *Planet. Int.*, 283, 82-91, <https://doi.org/10.1016/j.pepi.2018.08.006>.

356 Tsushima, H., R. Hino, Y. Tanioka, F. Imamura, and H. Fujimoto (2012), Tsunami waveform  
357 inversion incorporating permanent seafloor deformation and its application to tsunami  
358 forecasting, *J Geophys Res Solid Earth*, 117, B03311, 10.1029/2011JB008877.

359 Uehira, K., Kanazawa, T., Noguchi, S., Aoi, S., Kunugi, T., Matsumoto, T., Okada, Y., Sekiguchi,  
360 S., Shiomi, K., Shinohara, M., & Yamada, T. (2012). Ocean bottom seismic and tsunami  
361 network along the Japan Trench. In: Abstract OS41C-1736 presented at 2012 Fall Meeting,  
362 AGU.

363 Yamamoto, N., S. Aoi, K. Hirata, W. Suzuki, T. Kunugi, and H. Nakamura (2016), Multi-index  
364 method using offshore ocean-bottom pressure data for real-time tsunami forecast, *Earth,*  
365 *Planets and Space*, 68(1), 128, doi:10.1186/s40623-016-0500-7.

366

367

368

369

370

371

372

373

374

375

376

377

378

379

380

381

382 **Figure Captions:**

383 Figure 1. Bathymetry of the study area and locations of the S-net sensors (red dots). The red  
384 rectangle shows the source area of the 17<sup>th</sup> century giant earthquake (Mw 8,8), according to  
385 Ioki and Tanioka (2016). The black rectangle shows the source area of the 1973 Nemuro-oki  
386 earthquake (Mw7.8), as per Tanioka et al. (2007).

387  
388 Figure 2. Tsunami simulation area and locations of the calculated assimilation data (red dots) using  
389 interpolation of the observed data at the S-net sensors (black dots). The blue and green  
390 rectangles show the locations of the two test fault models of the hypothetical giant earthquake  
391 (Mw8.8) and the Nemuro-oki earthquake (Mw8.0), respectively. Triangles demarcate the  
392 locations where the tsunami waveforms are compared in Figures 4 and 6.

393  
394 Figure 3. Comparisons of the tsunami height fields at 90 and 1200 s after the initiation of the  
395 earthquake for the reference tsunami of the giant earthquake and three assimilation tsunamis  
396 as computed by the interpolation of the simulated observation data at the S-net sensors using  
397 Eq. (3), where control factors  $\alpha$  from Eq. (4) ranges from 1 to 3.

398  
399 Figure 4. Comparisons of tsunami waveforms at seven locations (refer to Figure 2 for exact  
400 locations) for three assimilation tsunamis (red lines) with the reference tsunamis (black lines)  
401 of the giant earthquake case, where control factors  $\alpha$  from Eq. (4) ranges from 1 to 3.

402  
403 Figure 5. Comparisons of tsunami height fields at 90 and 1200 s after the initiation of the  
404 earthquake for the reference tsunami (a) of the Nemuro-oki earthquake and two assimilation

405 tsunamis computed using the interpolation of the simulated observation data at the S-net  
406 sensors for a large assimilation area (b) (for exact locations refer to Figure 2) and a the small  
407 assimilation area (c) (for exact locations refer to Figure 7).

408  
409 Figure 6. Comparisons of tsunami waveforms at seven locations (refer to Figure 2 for exact  
410 locations) for two assimilation tsunamis (red lines) using (a) a large assimilation area (for exact  
411 locations refer to Figure 2) and (b) a small assimilation area (for exact locations refer to Figure  
412 7). The reference tsunami waveforms are shown by black lines.

413  
414 Figure 7. Locations of the assimilation data in a small assimilation area (marked by red dots)  
415 calculated by the interpolation of the observed data at the S-net sensors (black dots). The blue  
416 rectangle shows the test fault model of the Nemuro-oki earthquake (Mw8.0). Triangles  
417 demarcate the locations of the tsunami waveforms from Figure 6.

418  
419 Figure 8. Tsunami assimilation using the largest assimilation area for the giant earthquake. a)  
420 locations of the hypothetical assimilation points (red dots) and the S-net sensors (black dots).  
421 The blue rectangle shows the location of the fault model for the hypothetical giant earthquake  
422 (Mw8.8). b) the tsunami height fields at 90 s after the initiation of the earthquake for  
423 assimilation tsunami as computed by the interpolation of the simulated observation data at the  
424 S-net sensors. c) comparison of tsunami waveforms at seven locations (green triangles in (a))  
425 for two assimilation tsunamis using a large assimilation area (black lines, the same as Figure  
426 4) and the largest assimilation area (red lines) for the giant earthquake using the control factor  
427  $\alpha=2$ .

428

429 Table 1. Fault models for the two test earthquakes

Test fault model	Fault length (km)	Fault width (km)	Strike (°)	Dip (°)	Rake (°)	Slip (m)
Giant Eq. (Mw8.8)	300	100	228	15	90	15.0
Neumuro-oki (Mw8.8)	100	80	240	15	90	4.0

430

431 Table 2. Comparison of the maximum tsunami heights at seven locations computed from the  
 432 reference tsunami of the giant earthquake (Mw8.8) and the assimilations using the interpolation  
 433 where control factors  $\alpha$  ranges from 1 to 3 (see Figure 4). The ratios of the maximum tsunami  
 434 heights are indicated in parentheses.

Location	Reference	$\alpha=1$	$\alpha=2$	$\alpha=3$
	Max. heights (m)	Max. heights, (ratio) (m)	Max. heights, (ratio) (m)	Max. heights, (ratio) (m)
Hanasaki	13.6	3.93, (0.29)	14.2, (1.04)	14.9, (1.10)
Kushiro	10.5	7.99, (0.76)	10.8, (1.03)	15.2, (1.45)
Hiroo	17.8	8.88, (0.50)	21.2, (1.19)	28.0, (1.57)
Urakawa	4.21	1.69, (0.40)	3.96, (0.94)	4.92, (1.17)
Hachinohe	4.40	4.20, (0.95)	7.58, (1.72)	10.3, (2.34)
Miyako	5.79	3.54, (0.61)	6.30, (1.09)	7.99, (1.38)
Kesennuma	2.84	2.80, (0.99)	2.77, (0.98)	3.37, (1.19)
Average	8.45	4.72, (0.64)	9.54, (1.14)	12.1, (1.46)

435

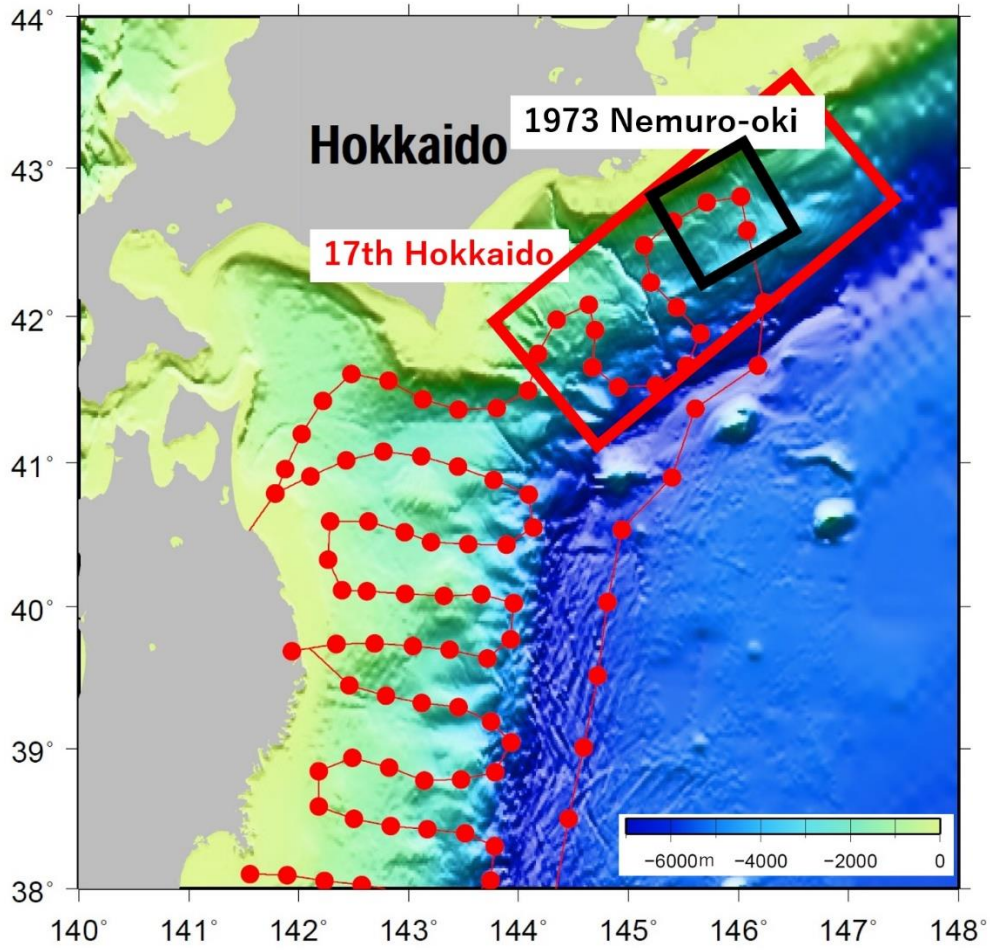
436 Table 3. Comparison of the maximum tsunami heights at seven locations computed from the  
 437 reference tsunami of the Nemuro-oki earthquake (Mw8.0) and the assimilations using the large  
 438 and small assimilation areas (for their location refer to Figure 6). The ratios of the maximum  
 439 tsunami heights are indicated in parentheses.

Location	Reference	Large assimilation area	Small assimilation area
	Max. heights (m)	Max. heights, (ratio) (m)	Max. heights, (ratio) (m)
Hanasaki	3.58	2.82, (0.79)	2.77, (0.77)
Kushiro	0.94	2.12, (2.26)	1.32, (1.40)
Hiroo	1.33	1.87, (1.41)	1.57, (1.18)
Urakawa	0.35	0.30, (0.86)	0.58, (1.66)
Hachinohe	0.60	1.17, (1.95)	1.12, (1.87)
Miyako	0.88	1.44, (1.64)	1.39, (1.58)
Kesennuma	0.39	1.02, (2.62)	0.78, (2.00)
Average	0.98	1.53, (1.65)	1.36, (1.49)

440

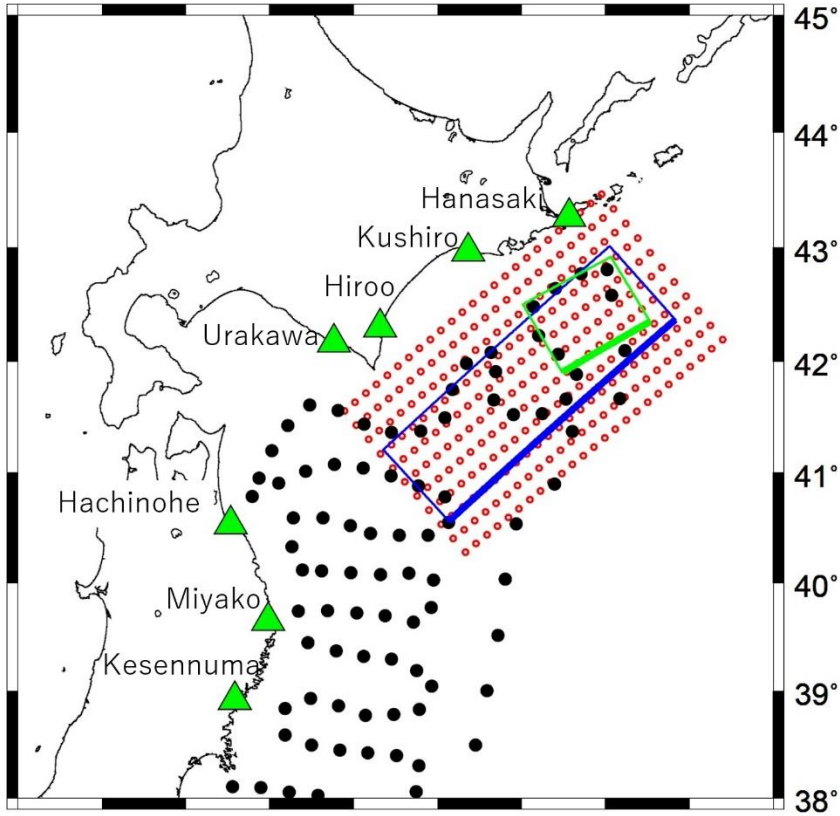
441

442



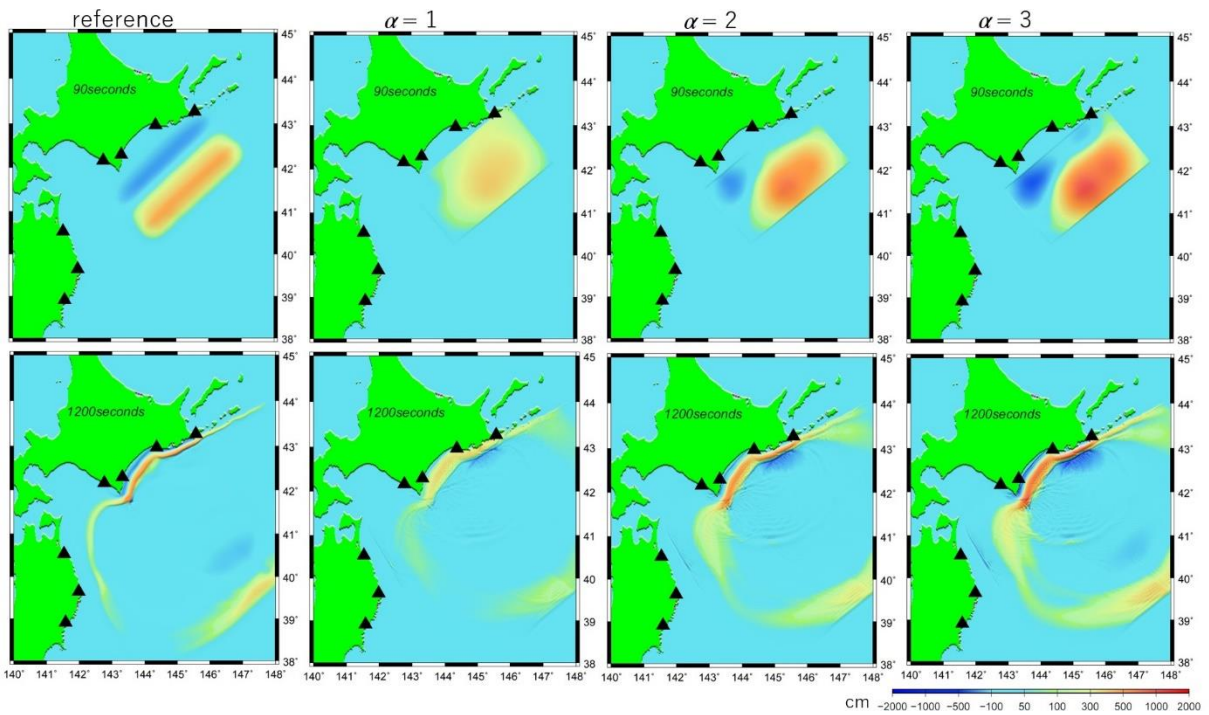
443

444 Figure 1.



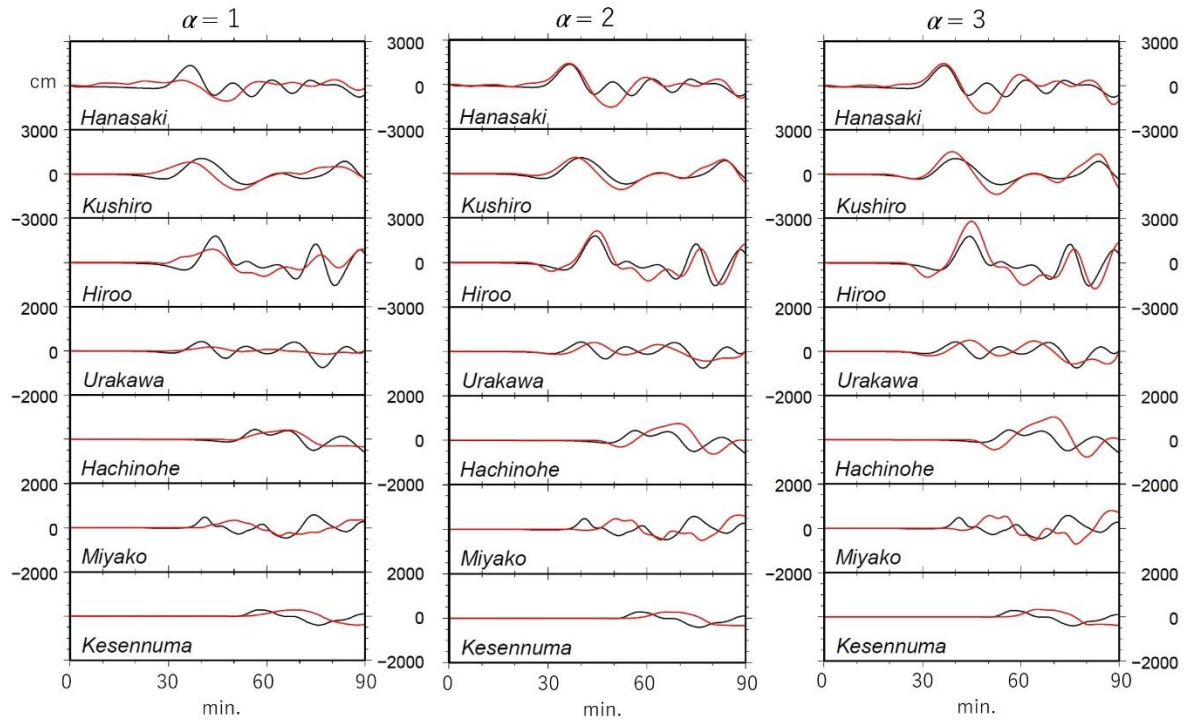
445 139° 140° 141° 142° 143° 144° 145° 146° 147° 148°

446 Figure 2.

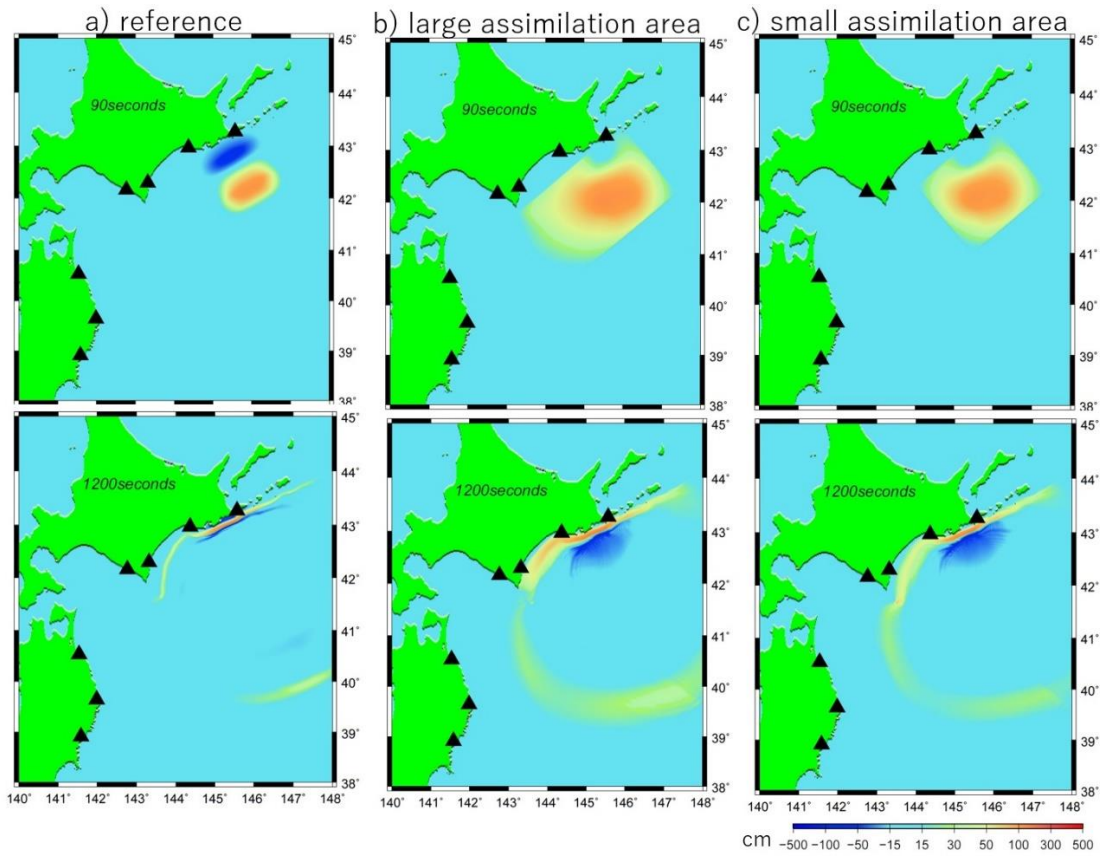


447

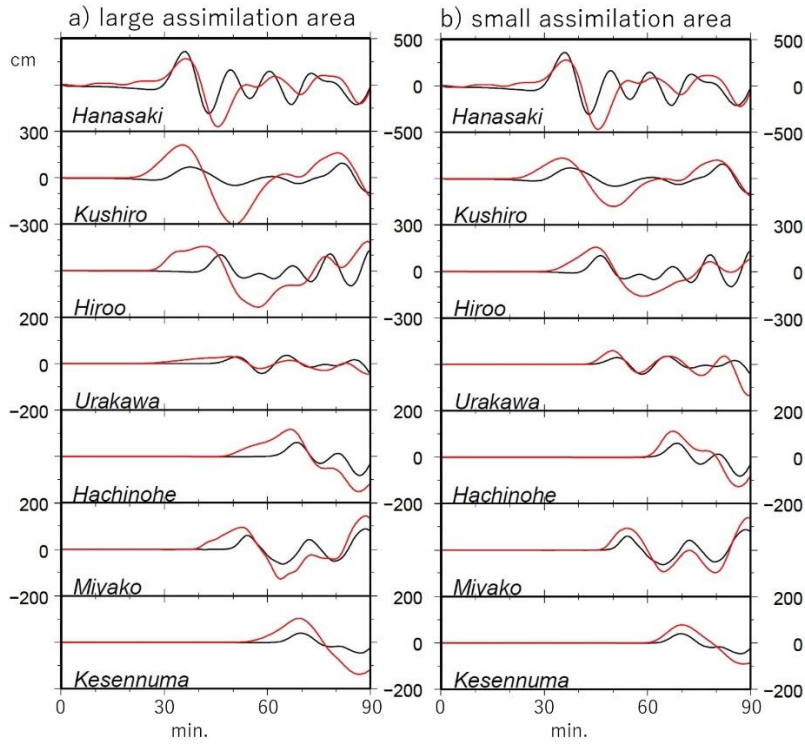
448 Figure 3.



449  
450 Figure 4.

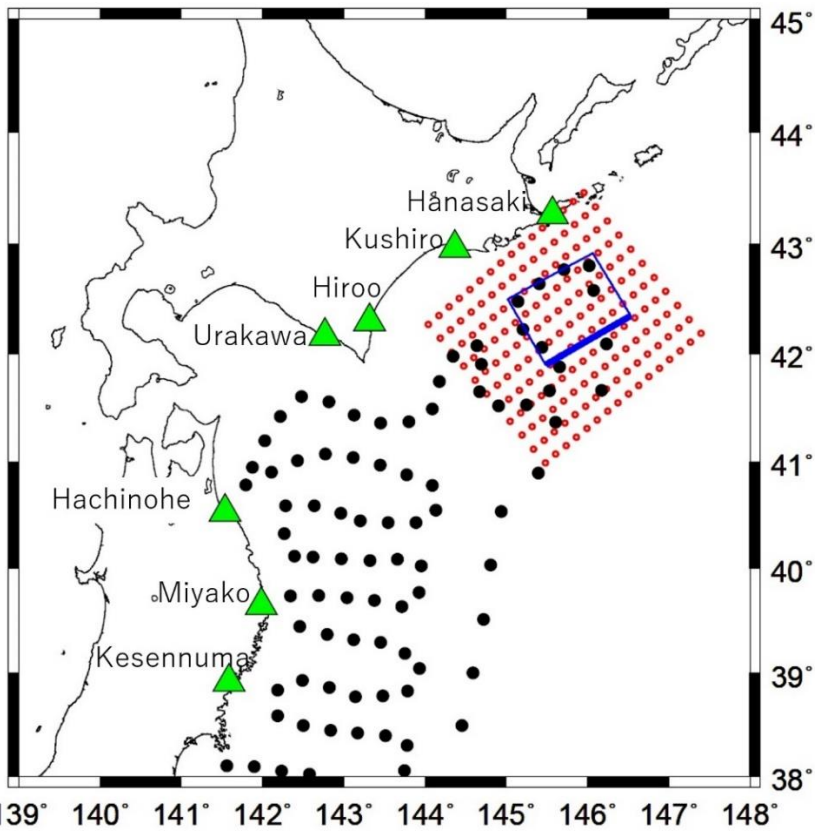


451  
452 Figure 5.



453

454 Figure 6.

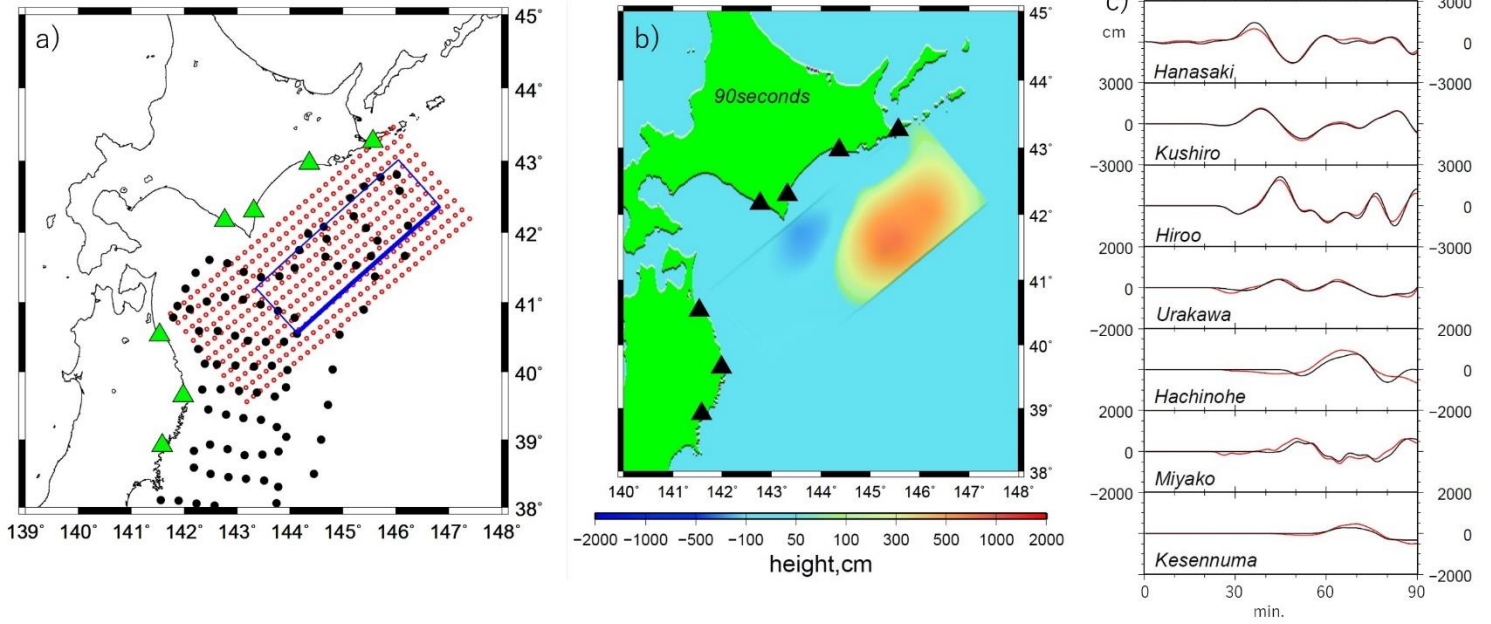


455

456 Figure 7.

457

458



459

460 Figure 8